International Journal of Fatigue 175 (2023) 107822

Contents lists available at ScienceDirect

International Journal of Fatigue

journal homepage: www.elsevier.com/locate/ijfatigue

Fatigue delaminations in composites for wind turbine blades with artificial wrinkle defects

Heloisa Guedes Mendonça [a,b,*], Lars Pilgaard Mikkelsen [a], Bing Zhang [c], Giuliano Allegri [c], Stephen R. Hallett [c]

[a] Department of Wind Energy, Technical University of Denmark, Frederiksborgvej 399, 4000 Roskilde, Denmark
[b] Vestas Wind Systems, Hedeager 42, 8200 Aarhus, Denmark
[c] University of Bristol, Bristol Composites Institute, Queens Building, Bristol BS8 1TR, United Kingdom

ARTICLE INFO

Keywords:
Wrinkle defects
Wind turbine blades
Composite materials
Fatigue damage
FEM

ABSTRACT

Out-of-plane wrinkles are manufacturing defects that affect the structural performance of wind turbine blades under fatigue. Glass Fiber Reinforced Polymer (GFRP) laminated specimens embedded with artificial wrinkle defects at two severity ratios (amplitude/half-wavelength) show different resistance to cyclic loading when tested under tension–compression fatigue. This work presents the validation of a fatigue formulation for the prediction of fatigue damage from wrinkles characteristic of wind turbine blades. The validation is performed through numerical models combined with experimental tests in which the fracture framework aims at predicting crack initiation and delamination propagation. The experimental fatigue program loaded the specimens with $R = -1$ to assess damage growth. The fatigue damage mechanism is quantified as a stiffness degradation, and the damage level is classified into five phases. Comparing the two severity types of wrinkles, the fatigue lifetime for equal external loading differs by approximately two decades. This difference is also captured by the numerical predictions. The lower the aspect ratio (AR), the higher the defect resistance to reversed fatigue loading. The numerical models captured the qualitative behavior of the SN curves and delamination fracture path and location observed in the experiments.

1. Introduction

In the context of global warming and the energy crisis, wind energy has emerged as a viable alternative to fossil fuels to achieve ambitious targets of zero carbon emissions. Development in wind turbine technology has been implemented to provide reliable and sustainable energy system generation. Wind turbine blades (WTB) are a major component of this system, with a complex composite structure comprising fiber-reinforced polymer-based laminates, balsa wood, and structural adhesives. Despite the technological advances in materials and structural efficiency, blade manufacturing is still mainly carried out through hand labor. In this way, defects such as wrinkles are prone to arise during production. Defects not detected during inspection remain in the structure, potentially leading to failure later during operation. Fiber wrinkling results from poor attachment of adjacent plies, in addition to low interlaminar shear strength [1]. The occurrence of out-of-plane wrinkles is frequent in composite structures [2]. Out-of-plane wrinkles result from fiber bending out of the laminate and ply bending through the thickness [3,4]. Another type of wrinkle is known as "s-shaped" or fold, with a maximum deviation of the fiber misalignment in which a layer comes into contact with itself [5]. Folds arise due to layup at the top of corrugated plies in regions of the mold with steep curvatures. In a wind turbine blade, this type of wrinkle usually arises at the root section. Characteristic parameters of wrinkles are wavelength (λ), amplitude (δ) and maximum angle (θ_{max}) (Fig. 1). The severity of the wrinkle can be measured by the aspect ratio (δ/λ) [6], maximum angle (θ_{max}) [7] or amplitude-to-thickness ratio (δ/t) [2]. In this work, a laminate representative of a wind turbine blade is embedded with out-of-plane wrinkles and a fold, in which the metric for severity will be the aspect ratio, i.e. amplitude to the half-wavelength ($2\delta/\lambda$).

The operation of a WTB with wrinkle defects can be detrimental, reducing the structure's lifetime. Regarding standards, there is a shortcoming in guidelines to certify composite structures with manufacturing defects. DNVGL-ST-0376 recommends the evaluation and material tests for blade structures with wrinkles at the most conservative failure mode [8]. Nevertheless, there are no specifications on the most conservative failure modes for different types of wrinkles at different load ratios. Few details exist on acceptable criteria to rule out or to put in operation a structure with such defects based on its severity

* Corresponding author at: Department of Wind Energy, Technical University of Denmark, Frederiksborgvej 399, 4000 Roskilde, Denmark.
E-mail addresses: hegmen@dtu.dk (H.G. Mendonça), lapm@dtu.dk (L.P. Mikkelsen).

https://doi.org/10.1016/j.ijfatigue.2023.107822
Received 27 April 2023; Received in revised form 14 June 2023; Accepted 3 July 2023
Available online 5 July 2023

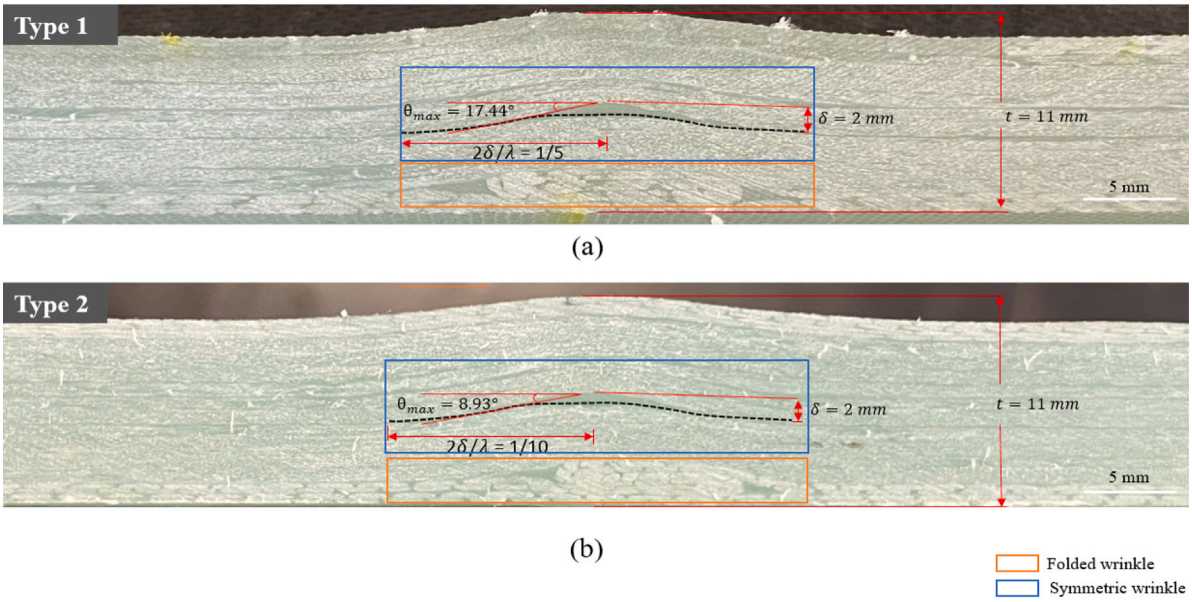

Fig. 1. Cross-section images of the specimens embedded with wrinkle defects (a) type 1 (AR = 1/5) (b) type 2 (AR = 1/10) in combination with respective geometrical dimensions, and the outlined regions for the folded and symmetric shape.

level. A number of studies have investigated the effect of wrinkles under quasi-static loading [7,9–14], but few have been applied to the wrinkles representative of a wind turbine blade [12–15]. Additionally, not many were dedicated to investigating the damage of wrinkles in composite structures. The fatigue life of a Glass Fiber Reinforced Polymer (GFRP) sandwich beam embedded with artificial wrinkles had the fatigue life reduced by 66% compared to a pristine laminate [16]. The investigation shows that in order to reach the target endurance, the fatigue load amplitude should be brought down to below 80% of the fatigue design limit. In [17], carbon fiber/epoxy (CFRP) laminates with out-of-plane wrinkles were tested under tension–tension fatigue at various load severities. The fatigue life of the wrinkle specimens at a given load severity was one order of magnitude below that obtained for specimens without wrinkles. Carbon-epoxy tape laminates with wrinkles are tested at constant loading amplitude with load ratio $R = 0.1$ to the point of failure onset and rapid delamination propagation ensued. In [18], fatigue failure initiation is observed at the resin pockets, followed by damage growth through the main wrinkle. The current study evaluates GFRP laminates with wrinkles at two load severity types under fully reversed loading, i.e. $R = -1$. The fatigue resistance and fracture behavior are investigated throughout.

Delamination is regarded as the main fracture mechanism in laminates with wrinkle defects under fatigue loading [16,17,19]. Nevertheless, a limited number of studies adopted numerical modeling in order to investigate the fracture mechanisms triggered by wrinkles. In this respect, some relevant literature contributions have been published by a research group based at the University of Bristol [20–22]. This approach entails implementing an energy-based Paris-type delamination propagation laws in a finite element (FE) framework to predict interlaminar and intralaminar fracture propagation in composite laminates. A crack-tip tracking numerical algorithm was proposed to investigate interlaminar fatigue crack growth within carbon fiber laminates with embedded artificial wrinkles [17]. Cohesive elements are inserted between each contiguous plies to describe progressive delaminations, and within plies to describe matrix cracks. A bilinear traction-separation law with interfacial stiffness degradation is considered for crack propagation, while the onset of the cohesive damage is detected by a quadratic stress interaction formulation. The 3D FE models are in good agreement with tension–tension fatigue tests $R = 0.1$. In [18], a fatigue damage progression algorithm is proposed, combining fatigue failure initiation criterion and variable stress for damage accumulation conditions. Linear damage accumulation is assumed, with stopping criteria for damage progression corresponding to a matrix crack of detectable size. Carbon epoxy tape laminates with embedded wrinkles were tested at three different wrinkle configurations at an $R = 0.1$, using DIC to measure the peak strains. The FE-models are built based on digital images of the defects and compared to the experimental tension–tension fatigue tests. Wrinkles were induced by a ply termination, which was later accounted for in the FE model. The modification of the model to account for ply-termination improved the predictions of failure location and number of cycles to failure. The objective of the current work is to investigate the fracture pattern of composite laminates with embedded wrinkles corresponding to the type of defects that are likely to appear in the manufacturing of wind turbine blades. A methodology for manufacturing the specimens in a defect-controlled manner is adopted, and the FE model is built accounting for the actual features of the cross-section image of the defect [14]. Given that this analysis aims at replicating a full-scale test of a wind turbine blade which locally is represented by a tension–compression loading of the laminates, a similar condition is implemented for the coupon specimens with an $R = -1$ for laminates with wrinkles of two different severity types. A FE modeling framework based on a user-defined cohesive implementation including a Paris-type law [22] predicts crack initiation and delamination propagation within the defect region. The number of cycles to failure, qualitative fracture behavior, stiffness degradation, and SN curves are considered as analysis parameters to verify the 3D FE modeling framework against the experimental campaign. At last, conclusions are drawn to improve the verification methodology adopted.

2. Experimental configuration

2.1. Artificial defects

The investigation was conducted with two types of wrinkles, where the severity metric is the aspect ratio amplitude to half-wavelength ($2\delta/\lambda$). The cross-sections and dimensions of the individual defects are shown in Fig. 1. Embedding the defects in the structure requires performing steps that can potentially lead to the formation of wrinkles when manufacturing a wind turbine blade. This step comprises the layup at the top of folded plies in regions of steep curvature as the root section. Consequently, a folded wrinkle is embedded at the start of the

layup, and a uniform wrinkle with prescribed geometrical parameters is further built into the structure. The specimens were manufactured using a defect control methodology outlined in previous work [14]. The technique consists of pre-curing a [0/0] panel to the shape of a mold casted to conform to the aspect ratio specified for the defect. The mold shaped defect emulates a uniform waviness. However, the nature of the manufacturing process results in laminates that are not identical and not perfectly symmetrical. At last, the pre-cured panel is stacked together at the center of the specimen along with UD (unidirectional) and Biax (biaxial) plies in a $[+45/-45/0/0/0/0/0]_s$ layup. A vacuum-assisted resin infusion (VARI) process impregnates the plies with resin, in which Hexion epoxy resin is applied in a mixing ratio of 100/28 by weight. The curing process follows a cycle of 12 h at 40 °C and 10 h at 80 °C. Once cured, the specimens are similarly trimmed in dimensions of 400×25 mm^2 with a thickness of 11 mm. The entire batch of samples is then submitted to a surface treatment process using sandpaper for polishing rough edges and a final lacquer acrylic cover as a finishing agent. This surface treatment is required to improve image analysis, with the additional effect of preventing rough borders from triggering premature delamination at the edges during the fatigue loading.

2.2. Fatigue tests

The objective of the experiment, other than generating the SN curves for high cycle and low cycle fatigue, was to capture the fatigue damage progression triggered by defects at different severity types and evaluate the fatigue damage mechanism of each defect type. This is accomplished through the fatigue test, during which fatigue damage is observed via video recording. Hence, the study aims to predict the location of the dominant fatigue-driven delamination, underlying the failure mechanisms rather than focusing on generating precise SN curves.

For the test configuration, coupon specimens are mounted in a test rig with a servo-hydraulic machine Instron 1333, with a load cell of 250 kN capacity. The experimental instrumentation comprises two consumer-grade Nikon D7500 cameras facing the side and back of the specimen, and an Optris P640 thermo-camera facing the side of the wrinkle as shown in Fig. 2. Five specimens for each wrinkle severity (type 1 and type 2) are tested for failure under tension–compression fatigue loading. The specimens are assembled into the hydraulic grips with two extensometers of 25 mm gauge length mounted back-to-back, aligned 40 mm away from the wrinkle center. Gauge lengths of 160 mm and 180 mm are used for wrinkle coupons type 1 and type 2 in the test grips, respectively.

The experimental program runs in load-control mode at $R = -1$ to derive the SN curves for each of the two severity levels. The linear strain, provided in Table 1, is determined through the E-modulus and stress, considering the cross-sectional area under the extensometers and the applied load. The program entails a constant load amplitude regime with a test frequency of 3 Hz at 0.25% amplitude, adjusted accordingly to the subsequent tests to keep the maximum strain rate constant. The load amplitude varies accordingly to determine data-points within N in $[1 \times 10^4, 3 \times 10^6]$. The specimens are tested at different load levels, as shown in Table 1. The initial stiffness of each specimen is measured at the beginning of each experiment by the slope of the stress vs. strain relation obtained by increasing the load at a constant rate until the defined test amplitude. The linear strain is then derived from the load amplitude and measured E-modulus. The actual strain is measured through extensometers. The program is defined to acquire 100 photos per decade of cycles. Additionally, photos were taken once the stiffness of each sample changed by more than 0.5%. The stiffness measurements for the specimens and material are recorded at the flat region. A limit of 3×10^6 cycles were used as the stop criterion. Had no cracks/stiffness drop been noticed after that given number of cycles, the specimen was considered a runout.

Table 1
Identification of wrinkle specimens linked to the percent strain amplitude.

Specimens Type 1 (WT1)		Specimens Type 2 (WT2)	
Strain amplitude [%]	Specimen ID	Strain amplitude [%]	Specimen ID
0.250	A-WT1	0.300	A-WT2
0.200	B-WT1	0.270	B-WT2
0.175	C-WT1	0.250	C-WT2
0.170	D-WT1	0.225	D-WT2
0.165	E-WT1[a]	0.215	E-WT2

[a]This specimen is a run-out with a test terminated after 3 million cycles.

The test was conducted while several stages of damage accumulation were observed until the final failure. The latter occurred because of a kink band at the wrinkle section and by a steep drop of stiffness. The crack path at the side and back of the specimens was captured by the Nikon cameras, while the thermo-camera detected the rise in temperature during the crack formation and propagation, see later in Fig. 5.

2.3. Experimental results

The evaluation of the test results comprises the analysis of the stiffness degradation and the SN curves for each of the two analyzed severity types at various strain amplitudes. The qualitative analysis for the fracture pattern is observed at every frame via the images captured by the camera. The stiffness degradation is shown in Fig. 3. Stiffness is derived from the linear regression in the stress-position curve and normalized by the initial position of the actuator. To draw the SN curves, the metric for failure is assumed as a stiffness decrease of 25%. A runout at 3×10^6 cycles is assumed for the specimens tested. That limit was detected at a strain amplitude of 0.165% for wrinkle type 1. The remaining specimens were tested and failed to below the established runout limit. The SN curves comparing both defect severities are displayed in Fig. 4. The crack propagation path is shown in Fig. 5, taken at a strain amplitude of 0.175% for the wrinkle type 1, whereas Fig. 6 displays the fracture pattern sorted by phases in the stiffness degradation graph for the same coupon. The fracture pattern is detected via visual inspection of the time-lapse images and observation of temperature changes registered by the thermo-camera.

Qualitative analysis is conducted at the set of time-lapse images captured along the experiment. A similar crack behavior was observed for the other specimens at both severity types after evaluating the images acquired by the Nikon camera and the thermo-camera. The loss of stiffness is noticed before the point where the slope of the curve drops considerably. The observed slight degradation in stiffness during the experiments supports the assumption of envelope displacement as linear strain remains quasi-constant throughout the experiment. In Fig. 5 and Fig. 6 it is possible to identify initial delamination denoted as Phase B at the interface Biax/UD around the folded wrinkle in the axial direction. Through the width, tunneling cracks grow lined up with the direction of the biaxial fibers. In the Phase C, the delamination path switches to the UD/UD interface at the wrinkle located above the resin pocket. The interlaminar crack grows to a characteristic delamination critical length before evolving to phase D. The image recorded at the back side of the laminate display a shadow growing in the transverse direction,indicating matrix cracking across the laminate. In phase D, multiple delaminations are detected across the interfaces and matrix, together with cracks along the width within the wrinkle region. At last, the final failure is denoted as Phase E, and it occurs because of a kink-band formation along the slope of the symmetric wrinkle.

A rise in temperature is observed during the fatigue test, due to the hysteresis loss resulting from the frictional sliding of the interfaces during delamination. Although the temperature rise can affect the mechanical properties of composites materials, the rise is of approximately 15 °C from Phase A to Phase E, which is considered acceptable.

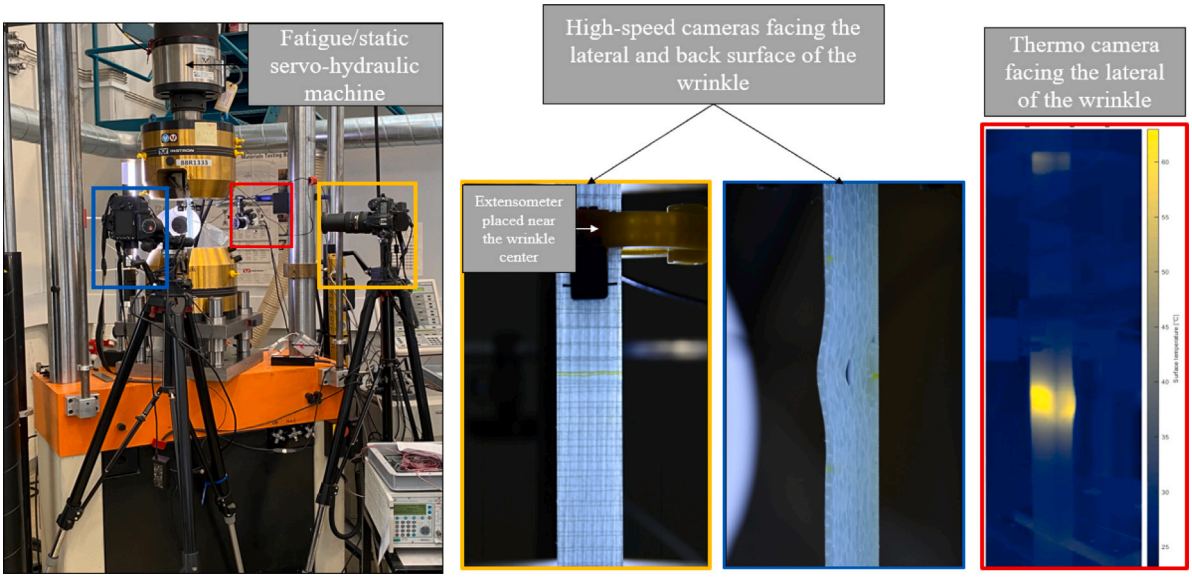

Fig. 2. Experimental test setup comprising high-speed cameras to track the crack start and delamination propagation path, thermo-camera faces the side of the specimen to track the gradient in temperature during the experiment.

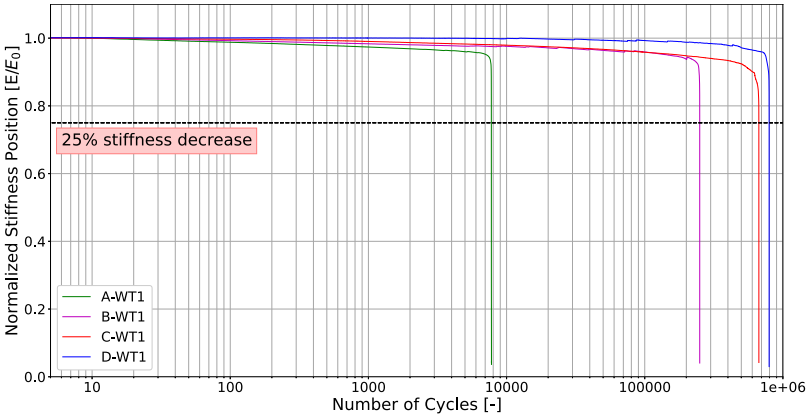

(a) Wrinkle type 1.

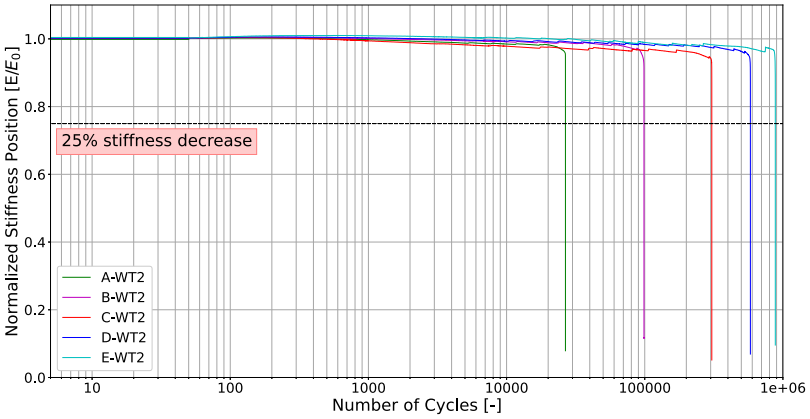

(b) Wrinkle type 2.

Fig. 3. Stiffness degradation normalized by the initial stiffness vs. cycles for wrinkle with severity type 1 and severity type 2 with a dashed line indicating the metric for failure at 25% stiffness drop.

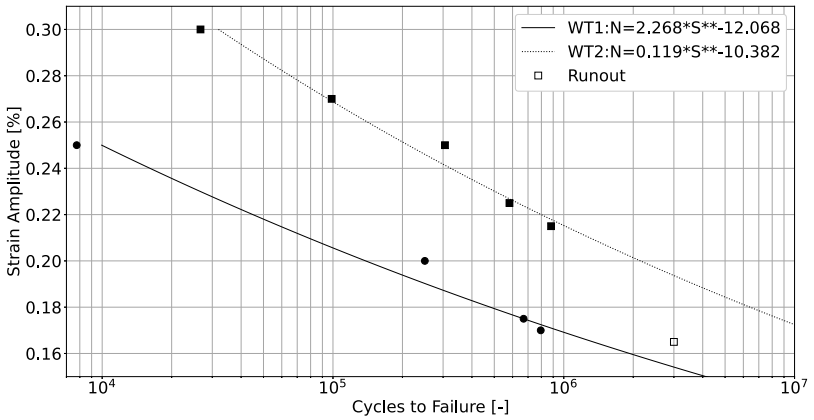

Fig. 4. Experimental SN Curves for Wrinkle Type 1 and Wrinkle Type 2.

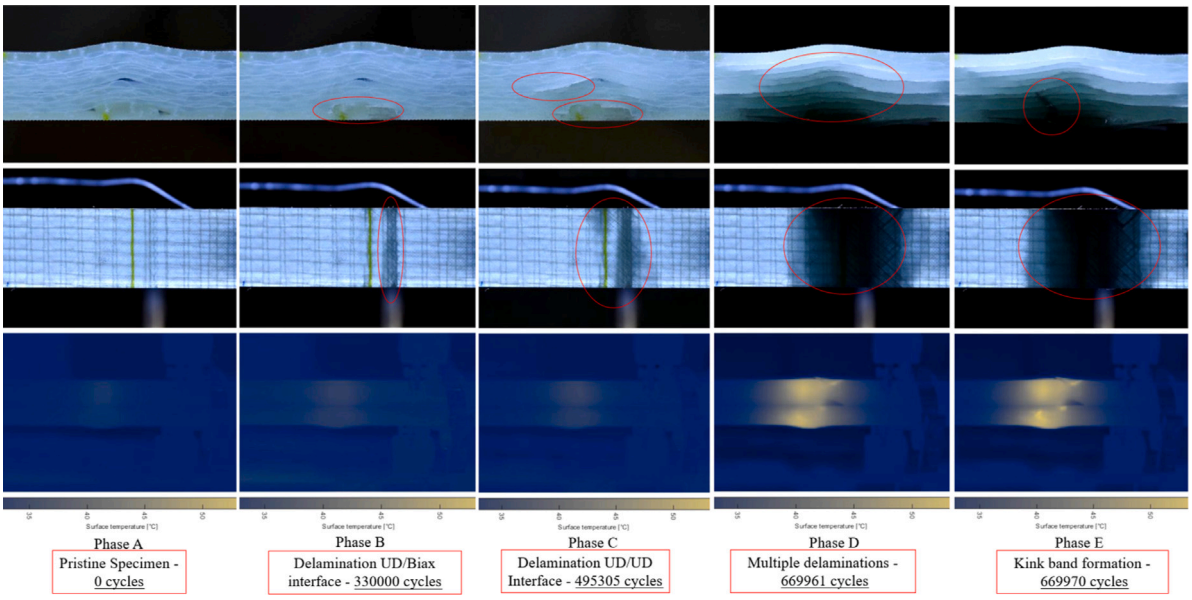

Fig. 5. Fracture phases identified during the fatigue loading within the wrinkle section taken from specimen ID C-WT1 with the temperature scale at the bottom of the image ranging within T [30:55 ° C].

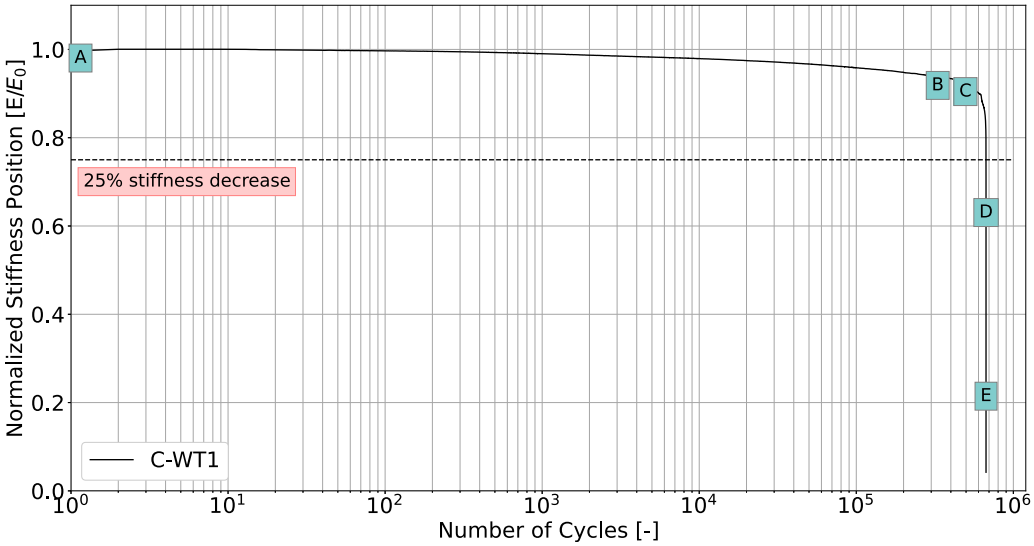

Fig. 6. Fracture phases displayed along the stiffness degradation chart for specimen ID C-WT1.

Moreover, the highest temperature of approximately 60 °C is detected in the late stage of multiple delaminations propagation in Phase D. Although the first delamination is observed in Phase B, one can notice a slight stiffness decrease between Phases A and B. This occurrence can be attributed to microcracks evolving within the structure, which may have gone undetected via visual or thermal inspection, or due to damage arising in the gripping section. Additionally, as the stiffness is measured by the piston position, the global degradation of the laminate is considered for the overall damage progression. This implies that not only the local degradation due to the wrinkles is considered, but also that the overall stiffness variation throughout the entire structure could contribute to the stiffness drop before Phase B.

One of the objectives of the present study is to measure and predict the failure introduced by the presence of wrinkles. However, it is worth mentioning that the experimental and numerical investigation of laminates without wrinkles has not been addressed in the current research. Evaluating a wrinkle-free laminate would require the implementation of a distinct test and modeling campaign designed to capture not only delamination but also other failure mechanisms, including matrix cracking and fiber failure.

The SN curves in Fig. 4 show that the laminate with wrinkle severity type 1 should operate at a strain amplitude below 0.170% to reach endurances in the order of 10^6 load cycles. The laminate with wrinkle type 2 can achieve the endurance at a strain amplitude below 0.215%. However, the runout for the wrinkle type 1 at a strain amplitude of 0.165% at 3×10^6 cycles indicates the high sensitivity of the defect lifetime to small variations on the load amplitude. Sensitivity to fatigue failure declines as the load amplitude decreases.

Isolating only the high cycle fatigue regime, the slope of the SN curve reduces, and the curves flatten at higher fatigue resistance. By considering specimen A-WT1 and specimen C-WT2 tested at the same strain amplitude, it is noticed that specimen A-WT1 fails at 2.5% of the fatigue life of specimen C-WT2. At 0.250% strain amplitude, the specimen at severity type 1 experiences a low-cycle fatigue regime. On the other had, the severity type 2 coupons behave accordingly to a high-cycle fatigue regime for the same load amplitude. The difference in lifetime between the wrinkles severity type 1 and type 2 for the same load amplitude is approximately two decades.

3. Finite element model

3.1. Constitutive law for fatigue

The fatigue cohesive formulation used for fatigue fracture growth is based on a bilinear static mixed mode cohesive law developed at the University of Bristol over several years within Bristol Composite Institute. A brief description of the model is described, and in depth details are referred to [20,23,24]. A formulation to evaluate delamination crack-propagation under cyclic loading is developed, linking the strain energy release rate at a cohesive interface to experimental Paris law data [20]. The cohesive interface constitutive law is based on the bilinear traction-displacement response (Fig. 7) for damage onset based on a quadratic damage criterion.

A power law is applied for complete decohesion and a static damage parameter tracks the accumulation of irreversible damage. The fatigue damage model relates damage accumulation law at the cohesive interface with Paris-type crack behavior. Interfacial stiffness is introduced as a parameter for the quasi-static loading (Step one) for delamination analysis. A fatigue initiation method based on SN curves and Linear Cumulative Damage (LCD) is set to detect damage onset [22]:

$$\left(\frac{\sigma_I}{\sigma_I^{max}}\right)^2 + \left(\frac{\sigma_{II}}{\sigma_{II}^{max}}\right)^2 = 1 - (s_I\psi_I^2 + s_I\psi_{II}^2)\cdot log(N) \tag{1}$$

where σ_I and σ_{II} are mode I and mode II tractions with its respective interface strength in those modes, σ_I^{max} and σ_{II}^{max}. Crack initiation parameters for mode I and mode II are given by s_I and s_{II} and extracted

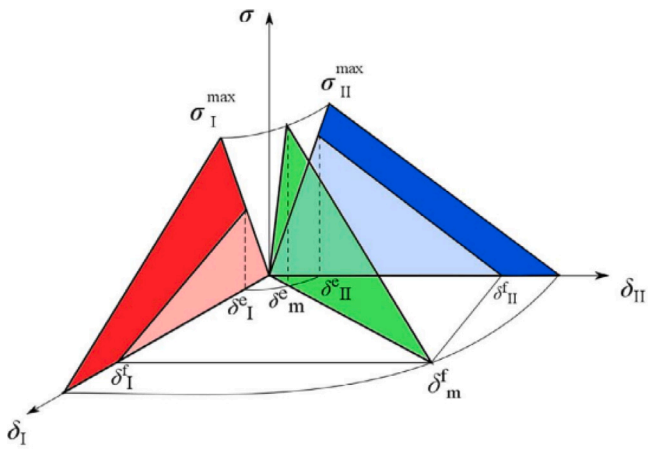

Fig. 7. Static mixed mode cohesive bilinear law [17,23].

from a semi-logarithmic plot of experimental data for tests in pure mode initiation [25]. N is the number of cycles, ψ_I and ψ_{II} are derived from the mode I, mode II, and mixed mode displacements:

$$\psi_I = \left(\frac{\delta_I}{\delta_m}\right)^2 \tag{2}$$

$$\psi_{II} = \left(\frac{\delta_{II}}{\delta_m}\right)^2 \tag{3}$$

The static damage variable is driven by the accumulation of irreversible damage:

$$d_s = \left(\frac{\delta_m - \delta_{m,e}}{\delta_{m,f} - \delta_{m,e}}\right) \tag{4}$$

where $\delta_{m,e}$ is the resultant displacement for damage initiation, δ_m is the mixed mode relative displacement and $\delta_{m,f}$ is the displacement for failure. Once d_s reaches the unity, the cohesive element enters the softening phase at the cohesive law reducing the interface strength. Complete failure occurs when the power law criterion reaches the unit:

$$\left(\frac{G_I}{G_{Ic}}\right)^{\alpha} + \left(\frac{G_{II}}{G_{IIc}}\right)^{\alpha} = 1 \tag{5}$$

where G is the energy release rate for modes I and II, and its critical value is indicated by 'c'. Fatigue damage variable is derived from crack propagation da/dN:

$$\left(\frac{da}{dN}\right) = C\left(\frac{G_{max}}{G_c}\right)^m \tag{6}$$

The mixed mode Paris law coefficient and exponent, C and m are derived from the experimentally measured values for Mode I and Mode II:

$$\begin{aligned} C &= \frac{G_I}{G_I + G_{II}}C_I + \frac{G_{II}}{G_I + G_{II}}C_{II} \\ m &= \frac{G_I}{G_I + G_{II}}m_I + \frac{G_{II}}{G_I + G_{II}}m_{II} \end{aligned} \tag{7}$$

At the maximum load, along with the static damage accumulated, an additional damage parameter is introduced for fatigue accumulation. Total damage is updated at every increment time as:

$$D_t = D_s + D_f \tag{8}$$

where D_t is the total damage, D_s is the static damage, and D_f is the fatigue damage. The cohesive damage law is implemented as a user material subroutine (VUMAT) in Abaqus/explicit and written in FORTRAN90. Damage, failure status, and number of cycles are saved

Table 2
Elastic properties for the GFRP and epoxy material [14].

	E_{11} (GPa)	E_{22} (GPa)	E_{33} (GPa)	G_{12} (GPa)	G_{13} (GPa)	G_{23} (GPa)	ν_{12}	ν_{13}	ν_{23}
UD	42.70	12.58	12.58	4.61	4.61	4.61	0.257	0.257	0.364
Biax [+45/−45]	13.92	13.92	13.92	11.5	11.5	5.53	0.533	0.533	0.257
Epoxy	3.2			1.2			0.3		

at each cohesive element as state variable for the entire analysis. The elastic properties for the resin epoxy, UD, and Biax plies are presented in Table 2 [14], and for fatigue damage in Table 3.

The data presented are representative of those for general glass/epoxy composite systems in the open literature. These data provide a reasonable basis for describing the phenomenon of fatigue-driven delamination via cohesive zone modeling. The properties for fracture toughness and Paris parameters (G_{Ic}, G_{IIc}, C_I, C_{II}, m_I, m_{II}) are based on Ref. [26]. Normal and shear traction strengths (σ_I^{max}, σ_{II}^{max}) are taken from experimental R-curves values investigated in [27]. The phenomenological damage variable for initiation (s_I, s_{II}) is based on values proposed at [22]. Studies prove the effect of through-thickness compressive stress on the enhancement of the Mode II fracture energy (G_{IIc}) corresponding result of the increase in the shear strength [28,29]. That effect is accounted for in a through-thickness enhancement factor, η. High penalty stiffness is introduced at the cohesive interface connecting the adjacent plies (K_I, K_{II}) [17].

3.2. Model definition

The response of the fatigue coupons is simulated using the finite element explicit solver Abaqus, version 2022. The model comprises UD and biaxial plies, along with resin epoxy pockets, which were described in Section 2.1. Three-dimensional eight-node linear brick elements with reduced integration (C3D8R) were used for the UD and biaxial plies. Six-node triangular prism solid elements (C3D6R) were used for the resin pockets. Eight-node cohesive elements (COH3D8) were used at the interface, as shown in Fig. 8. Cohesive elements are inserted between the plies to describe progressive delamination during the fatigue loading. Inter ply delamination was the main mode of failure included in this analysis. Although other mechanisms of fracture were observed during the experimental tests, the objective of the model is to track the critical delamination patterns and their location in the laminate. The finite element models take into consideration the real geometry of the defect cross-section. This implies that the resin pockets, folds, and wrinkles are geometrically built through an image processing of the defect cross-section image, as detailed in previous work [14] and hereby referred to as a high-fidelity geometric model.

A mesh sensitivity analysis was conducted in the models under fatigue loading, taking the number of cycles to failure as a metric for assessing the convergence of the analysis. As discussed in [17], the fatigue cohesive zone length tends to be smaller than the quasi-static cohesive length. Convergence is achieved at an individual element size of 0.35 mm and cohesive element layer thickness of 0.01 mm. The investigated FE models achieved convergence for a global mesh size of 0.2 mm and an interface mesh of 0.1 mm. The complete model consists of 8.7 million solid elements, including ply, resin, and cohesive elements. A discrete material orientation was assigned to each individual ply following their wavy contour. Therefore, material axis 3 follows the normal of the elements mid-plane, aligned with the curve representing each ply contour. Directions 1 and 2 are the global x and y directions. Constraints are introduced through kinematic couplings at reference points located at both ends of the model.

Displacement is applied at the reference point (main node) and transferred to the surface nodes positioned at the right end of the model (secondary nodes). Two loading steps analysis are performed according to the envelope load method described in [24] (Fig. 9), considering two pseudo-time steps at a pseudo-frequency (f). In the current work, displacement (D) is applied instead of load. Table 4 presents the differences in the test conditions compared to the numerical model specifications. In step one, a quasi-static analysis is conducted with smooth displacement increment ramping up from zero to the fatigue amplitude displacement, while fatigue is activated in step two, holding the displacement constant throughout the analysis. A limitation in the current implementation is that reverse loading with $R = -1$ is not covered. Thus, only a single bound of the envelope can be investigated at a time ($0 < R < 1$ and $1 < R < +\infty$). A critical factor in the performance of Abaqus/Explicit is the stability limit [30]. The conditional stability of the explicit method relies on the time increment, Δt. In the explicit solver, the time increment is typically short in order to guarantee numerical stability. Although the time increment unit is defined in seconds, it does not represent a physical meaning. The formulation links the analysis time (T) to the number of cycles (N), in which N = Tf. The kinetic and internal energy is used as a metric to evaluate the use of the mass scaling. From a mass scaling corresponding to a global stable time increment of $\Delta t = 10^{-5}$ s, the kinetic energy is sufficiently small and retained below 0.5% of the internal energy, which is kept constant until the point of delamination. Then the internal energy drops due to energy dissipation from delamination. Both models (defect type 1 and type 2) present approximately the same number of degrees of freedom, which results in a similar calculation time of ≈32 h performed in a 32 CPUs Linux cluster.

3.3. Numerical verification

This section presents the verification of the model results based on the following:

- Material sensitivity analysis on the fatigue properties effect on the behavior of the SN curves.
- Agreement of experimental SN curves for wrinkles at severity types 1 and 2 to the SN curves obtained from the fatigue simulations.
- Comparison of fracture phases identified in the experimental campaign to the fracture phases captured in the model.

The envelope displacement assumption in the cohesive fracture formulation is advantageous for computational performance. However, the models can only be evaluated at one side of the envelope at a time. The compression–compression fatigue load is considered critical for wrinkles, whereas tension–tension loading has a major impact on matrix cracks [31,32]. Therefore, the models are simulated in compression–compression, assuming a conservative fatigue sequence. The applied displacement amplitude is based on Table 1 and kept constant throughout the fatigue analysis. The applied displacement is obtained from the linear strain measured at the flat region of the specimens, where the extensometers are located.

Table 3
Fatigue properties for GFRP cohesive interface [17,22,26–29].

G_{Ic} [26] (J/mm^2)	G_{IIc} [26] (J/mm^2)	σ_I^{max} [27] (MPa)	σ_{II}^{max} [27] (MPa)	K_I [17] (N/mm^3)	K_{II} [17] (N/mm^3)	α (–)
0.26	1.00	40.3	23.4	10^5	10^5	1.2
s_I [22] (MPa/decade)	s_{II} [22] (MPa/decade)	C_I [26] (mm/cycle)	C_{II} [26] (mm/cycle)	m_I [26] (–)	m_{II} [26] (–)	η [28] (–)
0.075	0.15	0.00221	0.122	5.09	3.6	0.74

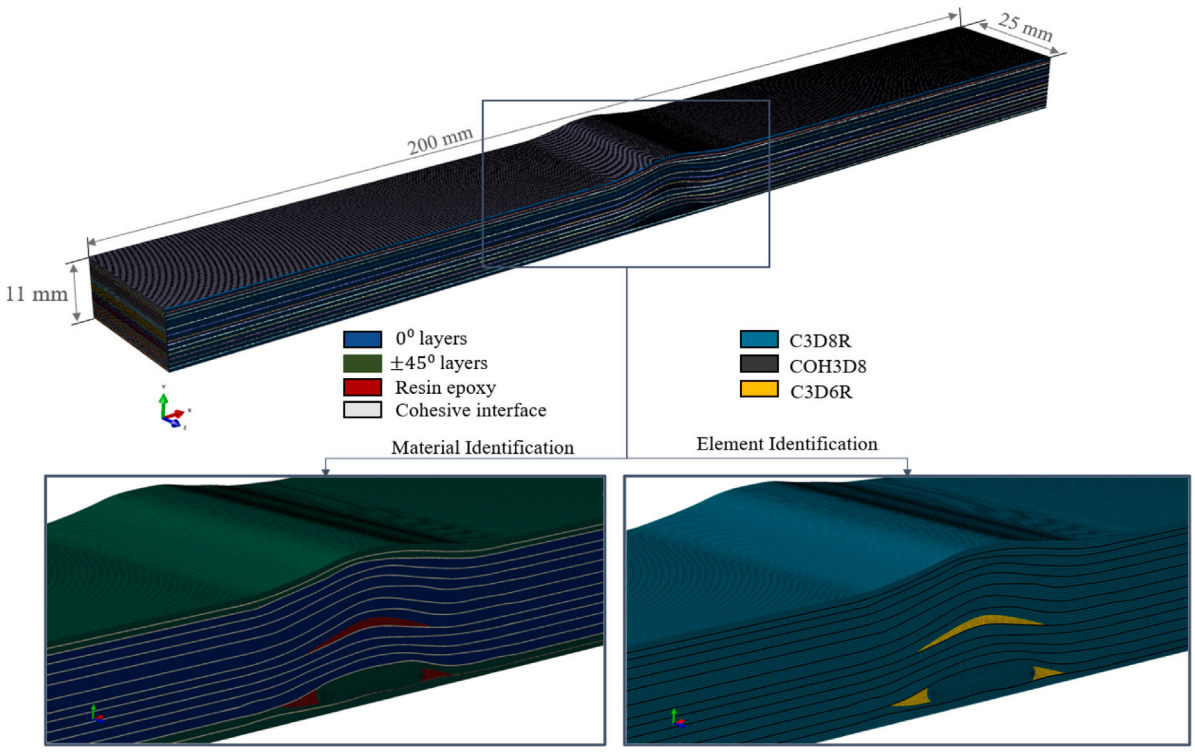

Fig. 8. Finite Element Model with material identification and the elements selected for ply, resin, and cohesive regions.

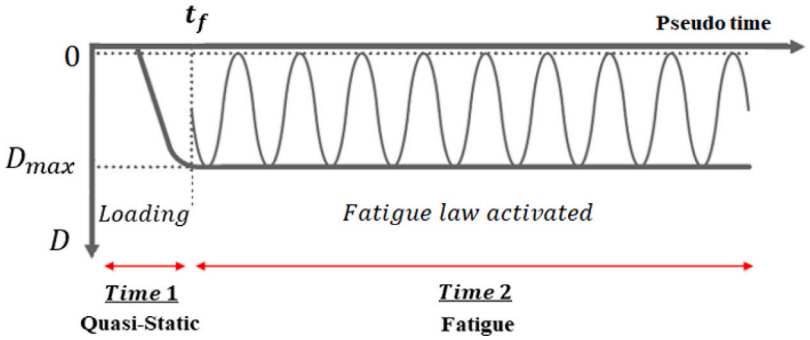

Fig. 9. Envelope displacement method [24].

Table 4
Comparing definitions for the exp. tests with the definitions with the numerical model specifications.

Experimental tests	3D numerical model
tension–compression	Compression–compression
Load-control	Displacement envelope
Strain amplitude	Strain amplitude is the strain range for compression

3.3.1. Fatigue properties sensitivity analysis

Material parametric analysis is conducted at different displacement amplitudes to evaluate the sensitivity of the interface fracture parameters on the qualitative behavior of the SN curves as shown in Fig. 10. The analysis is performed for the laminate with severity type 1 under compression–compression loading and modifying one parameter at a time from the Baseline material card presented in Table 3. The parameters are modified to cover values on the upper and lower limits of the baseline. The metric evaluation is the change in position and slope of the SN curve. As wrinkles act as local shear stress concentrators [11], Mode II parameters are considered critical for interlaminar failure within the defect region. Although Mode I parameters can influence crack opening in compression, the sensitivity analysis studies only the influence of Mode II parameters on the performance of the fatigue curves. Furthermore, it should be noted that crack growth in Mode I requires much less fracture energy compared to Mode II.

Decreasing the crack initiation parameter $s_{II} = 0.10$ MPa/decade, the position of the SN curve is shifted to the right, increasing the fatigue resistance by about 0.20 decades. Increasing this value to $s_{II} = 0.20$ MPa/decade has the opposite effect where the SN curve is shifted to the left, but the fatigue resistance decrease by a factor of 0.15 decades. The Paris exponent $m_{II} = 3.00$ moves the position of the SN curve to the left, while $m_{II} = 4.00$ shifts it to the right. The difference in fatigue life is about 0.30 decades lower and higher for $m_{II} = 3.00$ and $m_{II} = 4.00$, accordingly. The Paris constant $C_{II} = 0.022$ mm/cycle moves the SN curve to the right, and $C_{II} = 0.32$ mm/cycle moves it to the left, in which the difference in life compared to the Baseline is close to 0.20 decades. For the fracture toughness $G_{IIc} = 0.5$ (J/mm^2), the SN curve is shifted to the left with a difference close to 0.70 decades in the lifetime and $G_{IIc} = 1.5$ (J/mm^2) is shifted to the right to increase the fatigue life in about 0.35 decades. By evaluating the interface shear strength $\sigma_{II}^{max} = 13.40$ MPa shifts the curve to the left, and $\sigma_{II}^{max} = 33.40$ MPa shifts it to the right, but it displays a higher effect on the slope of the

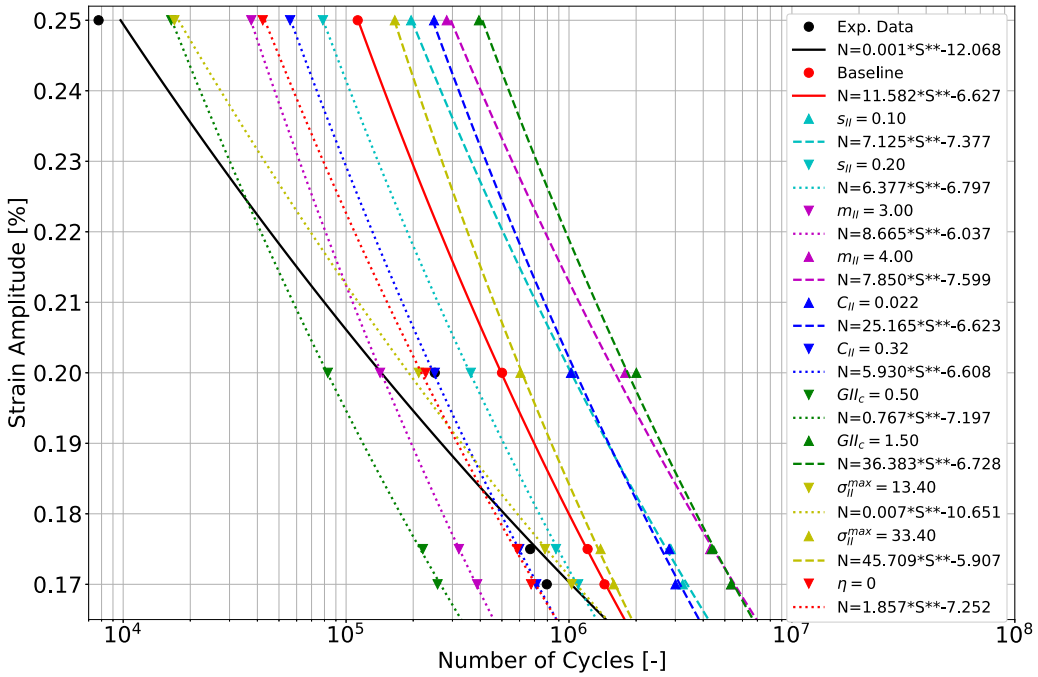

Fig. 10. Sensitivity Analysis for the fatigue interface properties.

Table 5
Influence of material parameters on the fatigue life.

Fatigue life increase	Fatigue life decrease
$\downarrow s_{II}$ $\downarrow C_{II}$ $\uparrow G_{IIc}$ $\uparrow m_{II}$ $\uparrow \sigma_{II}^{max}$ $\uparrow \eta$	$\downarrow \sigma_{II}^{max}$ $\downarrow m_{II}$ $\downarrow G_{IIc}$ $\uparrow s_{II}$ $\uparrow C_{II}$

curve, mainly when the value is decreased. Lower values of σ_{II}^{max} seem to have a stronger influence on high load amplitudes, indicating that at the low cycle, the initiation is the dominant effect. In contrast, for the high cycle, propagation is the dominant mechanism.

The difference in fatigue life varies accordingly, with the amplitude keeping fairly constant for the entire set of displacement amplitudes evaluated. Additionally, the effect of through-thickness compressive enhancement is disregarded in the analysis for $\eta = 0$. As observed in previous work [28], through-thickness compression increases the interlaminar shear strength. The difference in fatigue life is of 0.26 decades for the high load and 0.20 decades for low loads, indicating a strong influence on the shear strength enhancement for the low fatigue cycle.

In summary, the effect of fracture parameters on the fatigue life of wrinkle severity type 1 is presented in a qualitative overview compared to the Baseline parameters and displayed in Table 5. The values denoting an increase in fatigue life are symbolized with an upward arrow (↑), while those indicating a decrease are denoted by a downward arrow (↓).

3.3.2. Verification of SN curves

The global stiffness of the laminates in the model can be obtained from the reaction force during the fatigue loading normalized by the reaction force at the beginning of the fatigue analysis ($F/Fmax$). The baseline fatigue properties used for the verification are indicated in Table 3. Following the sensitivity analysis, a modification was made wherein $s_{II} = 0.20$ MPa/decade is assigned. It is worth mentioning that the interface properties used as a baseline in this work are derived from available data in the literature. In that way, a closer agreement can be found with a dedicated experimental campaign covering mode I, mode II, and mixed-mode tests for the particular material system being analyzed.

The SN curves set a drop of 25% in the global stiffness as a reference for failure (Fig. 11). At both severity levels, the compression–compression models predict a higher fatigue resistance compared to the experiments for $R = -1$. However, a higher difference in fatigue life is observed for high loads, which is noticeable when the low load cases are isolated in Fig. 12. Although model results present an overestimation of the number of cycles to failure for fatigue in compression, the predicted SN curves display the same qualitative behavior compared to the fatigue tests.

Despite different fracture mechanisms that occur between tension and compression loading, this analysis primarily focuses on the experimental observation that the compression part plays a dominant role in the fracture behavior. As a result, numerical investigation and determination of material parameters are focused on predicting the compression driven delamination failure mechanism. Fatigue phenomena affecting the bulk material represent a second order effect in terms of the structural integrity of the coupons. The failure is controlled by the presence of the wrinkle and the ensuing delamination. This is confirmed by the experimental data provided. Other fatigue damage mechanisms, notably tensile driven fatigue matrix cracking mechanisms, are assumed to have a negligible effect on the tension–compression fatigue of a wrinkled laminate and are therefore disregarded in this model. A fair agreement is observed when the high cycle fatigue cases are isolated, pointing to a better prediction of the model to low load fatigue. It can be justified by the modeling approach to cover the effect of delamination only. In this particular case, low cycle fatigue is matrix crack dominant, which is not covered in the model. Therefore, low cycle fatigue underestimates the effect of wrinkles on the fatigue lifetime.

The sensitivity analysis presented in Fig. 10 points to a better agreement of the data when the shear strength of the interface is reduced, which indicates the initiation is dominant for high load levels and the propagation dominates for low compression fatigue load levels. In that way, it seems that the interface properties are sensitive to the load level applied. As the predictions show fair agreement at high cycle fatigue, that could also point to a delamination driven fracture for low load cases.

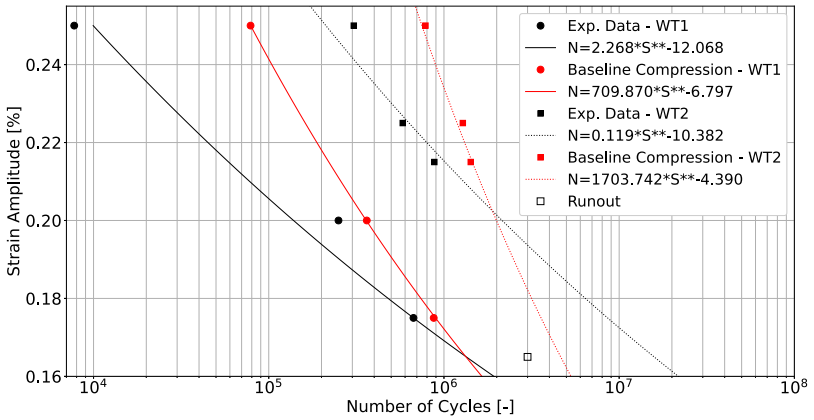

Fig. 11. SN Curves from numerical models and exp. data for the wrinkles at two severity types.

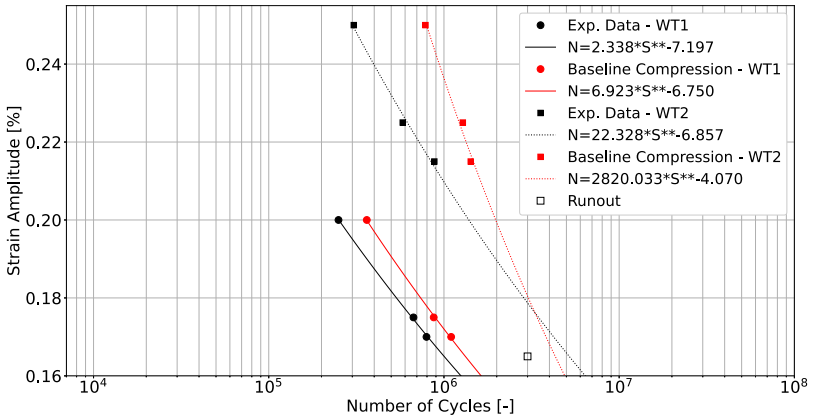

Fig. 12. SN Curves isolating high cycle cases for numerical models and exp. data for wrinkles at two severity types.

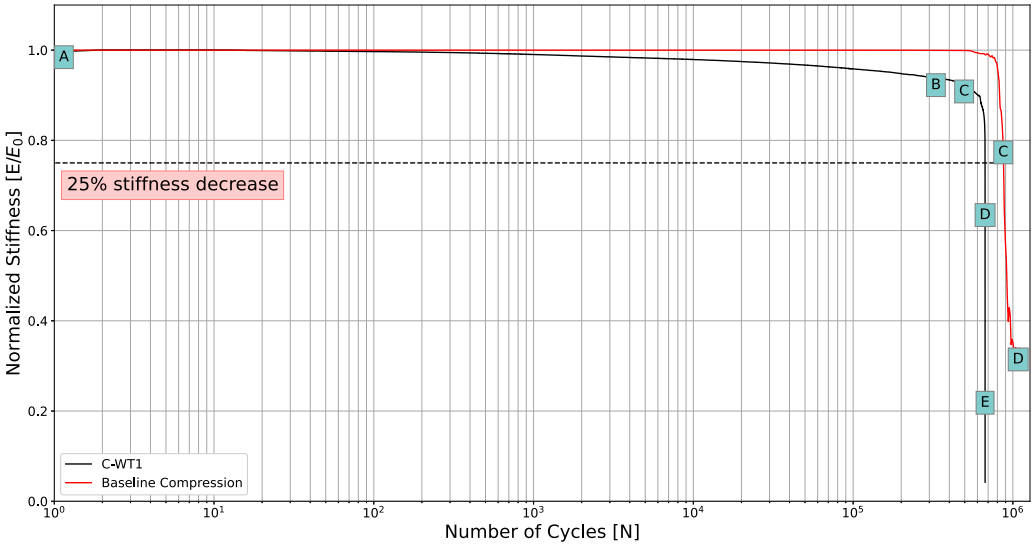

Fig. 13. Fracture phases represented in the stiffness degradation chart for specimen ID C-WT1 and analogous phases captured in the model for the same specimen.

3.3.3. *Verification of fracture phases*

Visual inspection of the samples and experimental time-lapse figures show that fracture phases are similar for both types of wrinkles at different load cases. Fig. 13 and Fig. 14 show the stiffness degradation curve and respective fracture phases which are captured in the model.

The prediction of phase C, where delamination in the UD/UD interface is observed in the tests, is equally captured by the model. Delamination at the interface Biax/UD around the fold is equally captured at that phase, although the initiation at that interface was not predicted by the model. Phase B was not captured in the model

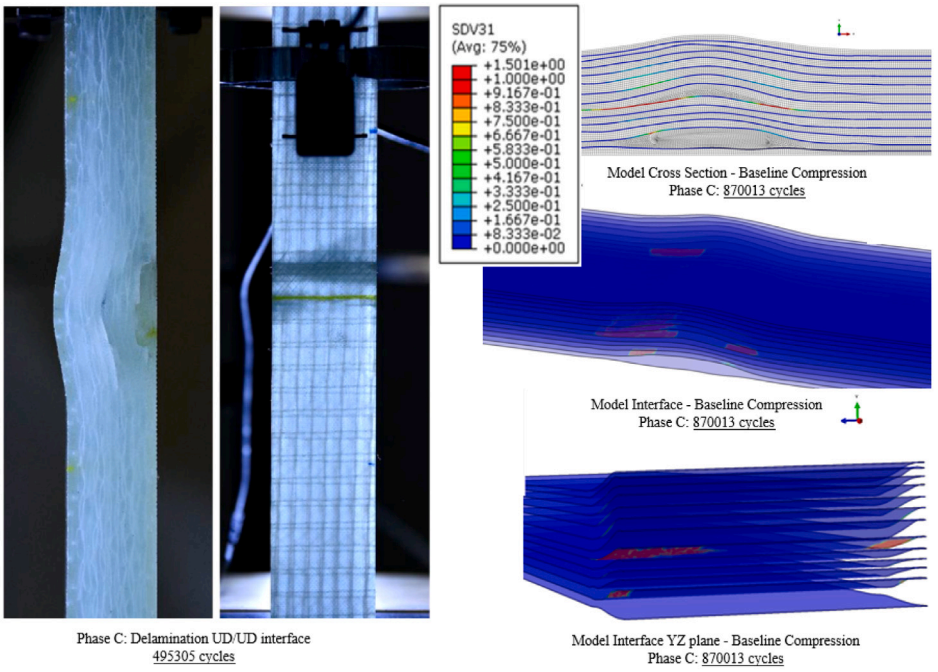

(a) Sample C-WT1 Phase C.

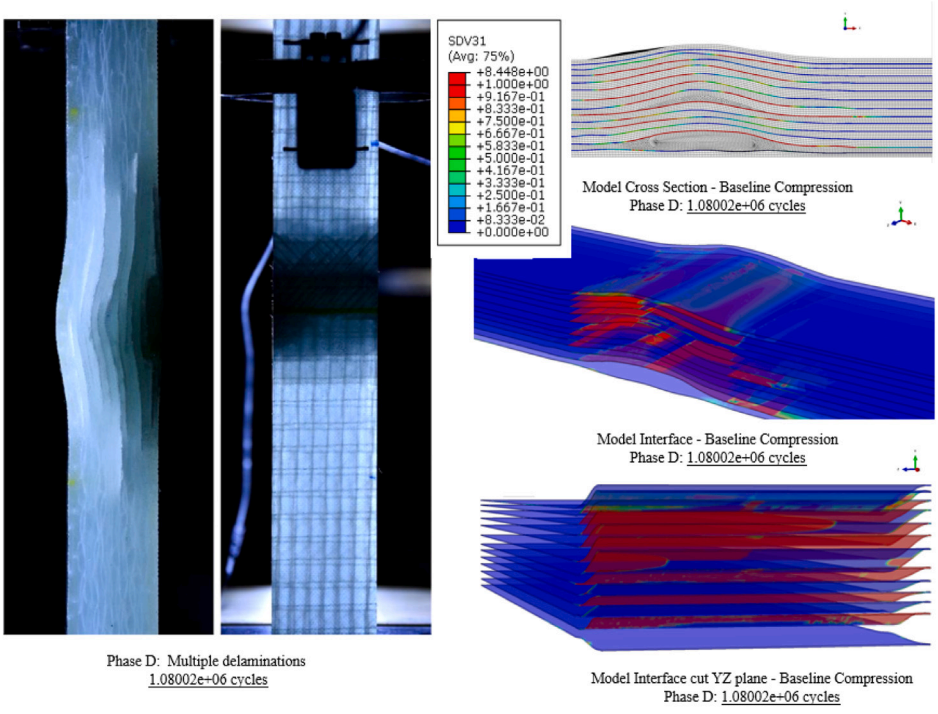

(b) Sample C-WT1 Phase D.

Fig. 14. Fracture modes model.

predictions as the model is not designed for interfiber failure in the form of transverse cracks. There are concentrations of resin around the fold, potentially leading to matrix cracking around that region. Phase D with multiple delaminations is captured in the model prior to the final failure with a kink band. The behavior of the stiffness degradation presents a similar pattern compared to the experiments. Stiffness degradation experimentally observed before the identification of several crack phases is not captured by the model.

4. Discussion and conclusion

This work presents the effect of wrinkles in representative laminates for wind turbine blades through a comparative analysis of two defect severity types under fatigue loading. The key contribution of this research lies in the investigation of the experimental SN curves for the defect types subjected to tension–compression fatigue loading with $R = -1$. Notably, wrinkles defects with equivalent amplitude but distinct aspect ratios exhibit a substantial sensitivity to fatigue life, in which higher aspect ratio specimens display inferior fatigue resistance. Additionally, an investigation into the fracture mechanism revealed that delamination predominates as the primary failure mechanism for this particular loading.

Furthermore, the present research introduces a numerical fatigue framework to evaluate fatigue fracture for the representative laminates. 3D numerical models representing the two defect severity types are verified using a Paris-law type fracture formulation, with delamination as the primary failure mechanism represented in the numerical analysis. The comparison between the numerical models and the experimental results indicates a fair agreement. Given its emphasis on delamination, the model presents an advantageous computational efficiency. Therefore, it may be feasible to employ this framework to investigate a representative section of a wind turbine blade using the same approach, with the focus solely on delamination as the governing failure mechanism of a wind turbine blade embedded with the same defect severity types. Different from the experiments, the numerical predictions are performed only using the compression side of the loading and under prescribed displacements, both of which will lead to a conservative lifetime prediction compared to the fully reversed and load-controlled cyclic loading experiments.

Experimental observations for fatigue test R = −1

- Initiation starts at the fold wrinkles around the resin pockets at the interface Biax/UD;
- Initiation seems driven by interfiber failure in the transverse direction;
- Delamination around UD/UD interface grows at the maximum amplitude wrinkle leading to multiple delaminations;
- Difference in fatigue life between the two severity types represents two decades.

Numerical Verification of the model:

- Sensitivity analysis with the interface parameters shows a change in the position of the SN curve for all the parameters, while only the shear strength of the investigated parameters essentially changes the slope;
- The Numerical model displays a fair agreement for high cycle compression–compression fatigue;
- Delamination phases and locations in the model are in agreement with the experiments, however, the initiation is not captured;
- Numerical SN curves and stiffness degradation present a fair qualitative agreement against the experiments.
- Low cycle fatigue seems initiation dominant, whereas high cycle fatigue seems propagation driven.

CRediT authorship contribution statement

Heloisa Guedes Mendonça: Conceptualization, Methodology, Software, Validation, Formal analysis, Writing – original draft, Writing – review & editing, Visualization. **Lars Pilgaard Mikkelsen:** Conceptualization, Writing – review & editing, Supervision. **Bing Zhang:** Software, Writing – review & editing, Supervision. **Giuliano Allegri:** Software, Writing – review & editing, Supervision. **Stephen R. Hallett:** Software, Writing – review & editing, Supervision.

Declaration of competing interest

The authors declare that they have no known competing financial interests or personal relationships that could have appeared to influence the work reported in this paper.

Data availability

Data will be made available on request.

Acknowledgments

The authors acknowledge the support from the Danish Energy Agency through the EUDP grant 64018-0068 in the ReliaBlade project. The authors also extend their appreciation to Fiberlab at DTU Wind and Energy Systems for conducting the experimental tests, with special mention to Steffen Rasmussen. Additionally, the authors would like to thank the team at Bristol Composites Institute, whose support was instrumental in completing this research.

References

[1] Bowles K, Frimpong S. Void effects on the interlaminar shear strength of unidirectional graphite-fiber-reinforced composites. J Compos Mater 1992;26(10):1487–509. http://dx.doi.org/10.1177/002199839202601006.

[2] Thor M, Mandel U, Nagler M, Maier F, Tauchner J, Sause MG, et al. Numerical and experimental investigation of out-of-plane fiber waviness on the mechanical properties of composite materials. Int J Mater Form 2021;14(1):19–37. http://dx.doi.org/10.1007/s12289-020-01540-5.

[3] Wang L. Effects of in-plane fiber waviness on the static and fatigue strength of fiberglass [Master dissertation], Bozeman: Montana State University, College of Engineering; 2001, URL https://www.montana.edu/composites/documents/LeiWangthesis.pdf.

[4] Lightfoot JS, Wisnom MR, Potter K. Defects in woven preforms: Formation mechanisms and the effects of laminate design and layup protocol. Composites A 2013;51:99–107. http://dx.doi.org/10.1016/j.compositesa.2013.04.004.

[5] Thor M, Sause MG, Hinterhölzl RM. Mechanisms of origin and classification of out-of-plane fiber waviness in composite materials—a review. J Compos Sci 2020;4(3):130. http://dx.doi.org/10.3390/jcs4030130.

[6] Wang J, Potter KD, Hazra K, Wisnom MR. Experimental fabrication and characterization of out-of-plane fiber waviness in continuous fiber-reinforced composites. J Compos Mater 2012;46(17):2041–53. http://dx.doi.org/10.1177/0021998311429877.

[7] Mukhopadhyay S, Jones MI, Hallett SR. Compressive failure of laminates containing an embedded wrinkle; experimental and numerical study. Composites A 2015;73:132–42. http://dx.doi.org/10.1016/j.compositesa.2015.03.012.

[8] DNV-GL. Rotor blades for wind turbines. Standard, Edition December, DNV-GL-ST-0376, 2015.

[9] Chun HJ, Shin JY, Daniel IM. Effects of material and geometric nonlinearities on the tensile and compressive behavior of composite materials with fiber waviness. Compos Sci Technol 2001;61(1):125–34. http://dx.doi.org/10.1016/S0266-3538(00)00201-3.

[10] Lee J, Soutis C. A study on the compressive strength of thick carbon fibre–epoxy laminates. Compos Sci Technol 2007;67(10):2015–26. http://dx.doi.org/10.1016/j.compscitech.2006.12.001.

[11] Mukhopadhyay S, Jones MI, Hallett SR. Tensile failure of laminates containing an embedded wrinkle; numerical and experimental study. Composites A 2015;77:219–28. http://dx.doi.org/10.1016/j.compositesa.2015.07.007.

[12] Bender JJ, Hallett SR, Lindgaard E. Parametric study of the effect of wrinkle features on the strength of a tapered wind turbine blade sub-structure. Compos Struct 2019;218:120–9. http://dx.doi.org/10.1016/j.compstruct.2019.02.065.

[13] Bender JJ, Hallett SR, Lindgaard E. Investigation of the effect of wrinkle features on wind turbine blade sub-structure strength. Compos Struct 2019;218:39–49. http://dx.doi.org/10.1016/j.compstruct.2019.03.026.

[14] Mendonça HG, Mikkelsen LP, Chen X, Bode J, Mortensen F, Haselbach PU, et al. Methodology to predict stiffness knock-down in laminates for wind turbine blades with artificial wrinkles. Wind Energy Sci 2022;7:2513–25. http://dx.doi.org/10.5194/wes-7-2513-2022.

[15] Leong M, Overgaard LC, Thomsen OT, Lund E, Daniel IM. Investigation of failure mechanisms in GFRP sandwich structures with face sheet wrinkle defects used for wind turbine blades. Compos Struct 2012;94(2):768–78. http://dx.doi.org/10.1016/j.compstruct.2011.09.012.

[16] Leong M, Hvejsel CF, Thomsen OT, Lund E, Daniel IM. Fatigue failure of sandwich beams with face sheet wrinkle defects. Compos Sci Technol 2012;72(13):1539–47. http://dx.doi.org/10.1016/j.compscitech.2012.06.001.

[17] Mukhopadhyay S, Nixon-Pearson OJ, Hallett SR. An experimental and numerical study on fatigue damage development in laminates containing embedded wrinkle defects. Int J Fatigue 2018;107:1–12. http://dx.doi.org/10.1016/j.ijfatigue.2017.10.008.

[18] Nikishkov Y, Makeev A, Seon G. Progressive fatigue damage simulation method for composites. Int J Fatigue 2013;48:266–79. http://dx.doi.org/10.1016/j.ijfatigue.2012.11.005.

[19] Murri GB. Influence of ply waviness on fatigue life of tapered composite flexbeam laminates. In: Composite structures: Theory and practice. PA, USA: ASTM International: West Conshohocken; 1999.

[20] Harper PW, Hallet SR. A fatigue degradation law for cohesive interface elements–development and application to composite materials. Int J Fatigue 2010;32(11):1774–87. http://dx.doi.org/10.1016/j.ijfatigue.2010.04.006.

[21] Kawashita LF, Hallett SR. A crack tip tracking algorithm for cohesive interface element analysis of fatigue delamination propagation in composite materials. Int J Solids Struct 2012;49(21):2898–913. http://dx.doi.org/10.1016/j.ijsolstr.2012.03.034.

[22] May M, Hallett SR. A combined model for initiation and propagation of damage under fatigue loading for cohesive interface elements. Composites A 2010;41(12):1787–96. http://dx.doi.org/10.1016/j.compositesa.2010.08.015.

[23] Jiang WG, Hallett SR, Green BG, Wisnom MR. A concise interface constitutive law for analysis of delamination and splitting in composite materials and its application to scaled notched tensile specimens. Internat J Numer Methods Engrg 2007;69(9):1982–95. http://dx.doi.org/10.1002/nme.1842.

[24] Tao C, Mukhopadhyay S, Zhang B, Kawashita LF, Qiu J, Hallett SR. An improved delamination fatigue cohesive interface model for complex three-dimensional multi-interface cases. Composites A 2018;107:633–46. http://dx.doi.org/10.1016/j.compositesa.2018.02.008.

[25] May M, Hallett SR. An assessment of through-thickness shear tests for initiation of fatigue failure. Composites A 2010;41(11):1570–8. http://dx.doi.org/10.1016/j.compositesa.2010.07.005.

[26] Blanco N, Gamstedt EK, Asp LE, Costa J. Mixed-mode delamination growth in carbon–fibre composite laminates under cyclic loading. Int J Solids Struct 2004;41(15):4219–35. http://dx.doi.org/10.1016/j.ijsolstr.2004.02.040.

[27] Erives R, Sørensen BF, Goutianos S. Extraction of mix-mode cohesive laws of a unidirectional composite undergoing delamination with large-scale fibre bridging. Composites A 2022;165:p.107346. http://dx.doi.org/10.1016/J.COMPOSITESA.2022.107346.

[28] Li X, Hallett SR, Wisnom MR. Predicting the effect of through-thickness compressive stress on delamination using interface elements. Composites A 2008;39(2):218–30. http://dx.doi.org/10.1016/j.compositesa.2007.11.005.

[29] Zhang B, Kawashita LF, Jones MI, Lander JK, Hallett SR. An experimental and numerical investigation into damage mechanisms in tapered laminates under tensile loading. Composites A 2020;133:p.105862. http://dx.doi.org/10.1016/j.compositesa.2020.105862.

[30] Li J, et al. ABAQUS documentation version 6.5 ABAQUS documentation version 6.5. ISIJ Int 2012;52(6):1072–9.

[31] Mikkelsen L. The fatigue damage evolution in the load-carrying composite laminates of wind turbine blades. In: Fatigue life prediction of composites and composite structures. Woodhead Publishing; 2020, p. 569–603.

[32] Jespersen KM. Fatigue damage evolution in fibre composites for wind turbine blades [Ph.D. thesis], DTU Wind Energy PhD-0075; 2017.